

While the addition of a modulator is generally expected to change crystal morphology, it can be difficult to predict the exact nature of that change. At a fundamental level, all MOFs can be described as being composed of Lewis acidic metal ions or clusters bridged by Lewis basic ligands that act as linkers. For the vast majority of reported frameworks, the organic linkers also behave as Brønsted-Lowry acids and/or bases during synthesis. Modulators with mimicking functionalities will also behave as Brønsted-Lowry acids or bases and change the protonation equilibrium in solution (pH in water or pH^* in nonaqueous media). Addition of modulators thus alters coordination and protonation equilibria simultaneously: increasing the concentration of modulator may increase competitive binding at metal sites, but it will also change the pH of the solution. Although this correlation has been described in the literature, the most common strategy employed to counterbalance these effects is the addition of a modulator followed by a pH-compensating Brønsted-Lowry acid or base, which increases the ionic strength of the solution.^{21–23} However, this strategy introduces a new variable into the reaction conditions, as the dramatic increase in ion concentration changes dissociation constants and reactant solubility.^{24–26} This complication is exacerbated by the solvothermal nature of many framework syntheses, in which linker deprotonation occurs via the thermal decomposition of an amidic solvent, most commonly *N,N*-dimethylformamide (DMF). In these syntheses, DMF will readily decompose at elevated temperatures to yield an amine and either a carbonyl species or a carboxylic acid via thermolysis or hydrolysis, respectively.²⁷ In this case, the solution pH and the number and identity of coordinating molecules change as a function of time, following a nonconstant and complex rate. The development of buffered, aqueous synthesis conditions would importantly enable deconvolution of the roles the modulator plays as a coordinative species and as a base.

The challenge of independently controlling pH and metal ion complexation has long been prevalent in biochemical and biological research. In 1966, Good and co-workers introduced a set of 12 buffers designed for use in biological studies near physiological pH,²⁸ among these are various zwitterionic *N*-substituted aminosulfonic acids. The buffers were selected based on a number of criteria, including the key requirement that the buffers do not coordinate metal cations or that they coordinate to form soluble salts with known binding constants. Indeed, controlling pH is necessary for the measurement of physiologically relevant properties, but for processes involving metallofactors, it is crucial that the buffer molecules do not preferentially form complexes with the metal ions. Given that metallofactors play an important role in regulating the kinetic and thermodynamic pathways of many biological processes,^{29–31} unintended metal complexation by buffer molecules can interfere with or fundamentally alter the physiological property being measured. Recognition that Good's molecules and a number of other common biological buffers can still engage in disruptive metal complexation motivated the identification of guidelines for optimal metal ion and buffer combinations³² as well as development of truly noncoordinating buffers.^{33,34}

The use of nominally or noncoordinating buffers similarly offers an intriguing means of controlling MOF crystal formation, given that most syntheses rely on the indirect and convoluted interplay of pH and metal complexation. The well-known series of frameworks $\text{M}_2(\text{dobdc})$ ($\text{M} = \text{Mg}, \text{Mn}, \text{Fe}, \text{Co}$,

$\text{Ni}, \text{Cu}, \text{Zn}, \text{Cd}$; $\text{dobdc}^{4-} = 2,5\text{-dioxido-1,4-benzenedicarboxylate}$; Figure 1)^{35–38} present an interesting test case in this

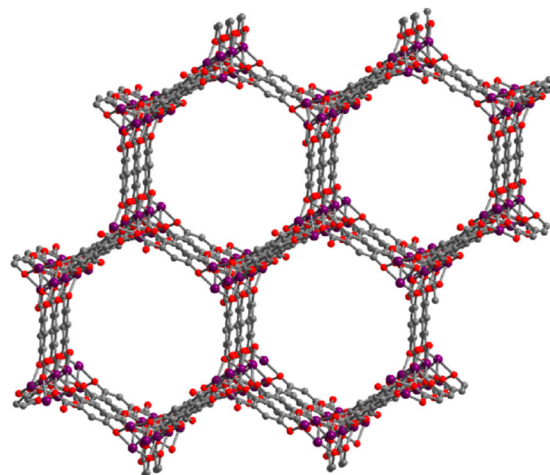


Figure 1. Portion of the crystal structure of $\text{Co}_2(\text{dobdc})$ illustrating the hexagonal pores along the *c*-axis. Purple, red, and gray spheres represent Co, O, and C atoms, respectively; H atoms are omitted for clarity.

regard. These materials feature a high density of coordinatively unsaturated metal(II) sites that can interact strongly and selectively with a variety of guest molecules and have accordingly been demonstrated as promising adsorbents for numerous gas separations applications.^{37,39–42} The traditional solvothermal routes used to prepare these frameworks generate either significantly polycrystalline samples or long rod-like crystallites, wherein the longest crystallite direction aligns with the one-dimensional channels propagating along the *c*-axis.^{43–52} Guest transport along the one-dimensional channels of the long crystals has been shown to be much faster than diffusion across the channels,⁵³ rendering much of the external surface inaccessible to molecules. Thus, developing a controlled means of synthesizing these crystals with optimal morphologies presents a highly desirable target.

Herein, we demonstrate that the synthesis of $\text{Co}_2(\text{dobdc})$ under mild conditions starting from cobalt(II) acetate results in the formation of regular, well-faceted single crystals that are compressed along the *c*-axis relative to crystals prepared via traditional routes. Use of a noncoordinating buffer to control pH during synthesis further reveals that acetate modulates crystal growth by competing with the dobdc^{4-} linker for coordination, a result that is borne out by computations. By varying the coordination strength of competing anion and the solution pH, it is possible to generate crystallites with varying sizes and morphologies, giving rise to a previously unprecedented level of control over framework crystal growth. Zero length column chromatography experiments demonstrate that diffusion of the industrially important molecule *m*-xylene is more favorable in crystals that are compressed along the *c*-axis, highlighting the importance of fine-tuned control over crystal growth for real-world applications.

RESULTS AND DISCUSSION

Morphology of Non-Buffered $\text{Co}_2(\text{dobdc})$. The synthesis of $\text{M}_2(\text{dobdc})$ has been reported in a range of solvent systems, including pure water,^{54,55} water/tetrahydrofuran mixtures, alcohol mixtures,^{56–58} and DMF.^{35,37} Since we

were interested in developing methods to probe the effects of pH and metal complexation separately, we chose to avoid DMF, which decomposes during synthesis, making it challenging to quantify base concentration at each point during the reaction. Water is a clear choice to enable a quantitative measure of pH; however, the low solubility of H_4dobdc in water would severely limit the maximum concentration of reactants in solution. The use of ethanol as a cosolvent with water promotes the solubility of all reactants while still enabling the quantitation of pH.^{59–61} Moreover, water/ethanol mixtures have the potential to offer more environmentally conscious syntheses for industrial applications. Finally, given the precedent for the use of acetate as a base in the synthesis of $M_2(dobdc)$ ($M = Co, Ni, Zn$),^{54,62,63} cobalt(II) acetate was selected as the metal precursor.

The nonbuffered synthesis of $Co_2(dobdc)$ was carried out by combining $Co(CH_3CO_2)_2 \cdot 4H_2O$ and H_4dobdc in a 1:1 (v/v) water/ethanol mixture in a 20 mL scintillation vial and heating the mixture to 75 °C in an oil bath for at least 2 h. These conditions yield readily dispersible orange crystalline particles, and powder X-ray diffraction data for this solid are consistent with the expected $Co_2(dobdc)$ phase (Figure S1). Optical microscopy characterization of the particles indicated that they have uniform size and morphology, and the uniform reflectance or transmittance of polarized light across individual crystallites showed them to be single crystals (Figure S2). Scanning electron microscopy (SEM) images of the crystallites revealed low-dispersity polyhedra with clearly defined facets (Figure 2a). We found that using an oven instead of an oil bath during synthesis produces slightly larger crystallites with much greater polydispersity (Figure S3). To ensure reproducibility and enable reliable comparison across all samples, all subsequent reactions were performed using an oil bath. Significantly, our synthesis route affords access to regular, well-faceted single crystals with a characteristic length of $\sim 10 \mu m$, which is important for obtaining accurate diffusion measurements (see below). In marked contrast, crystallites of $Co_2(dobdc)$ synthesized via the reported solvothermal route³⁷ using $Co(NO_3)_2 \cdot (H_2O)_6$ and a 1:1:1 (v/v/v) mixture of DMF, ethanol, and water generates clusters of long, rod-like crystallites (Figure 2b). Similarly, the preparation of $Co_2(dobdc)$ at room temperature starting from cobalt(II) acetate previously yielded nanoparticles on the order of 20 nm.⁶¹

The narrow-dispersity polyhedra resulting from synthesis in water/ethanol are pentagonal dodecahedra that are elongated along a 3-fold axis (Figure 3, left). Notably, the crystallites do not possess the expected long rod-like morphology. Instead, they exhibit a shorter, more truncated shape that is consistent with S_6 symmetry within the space group $R\bar{3}$.⁶⁴ The only 3-fold axis of symmetry apparent in the crystal morphology corresponds to the 3-fold c -axis found in $R\bar{3}$. A self-consistent set of Miller indices can be generated with symmetry operators and the correct choice of one of each of the side faces and the top face. Here, the $\{100\}$ and $\{401\}$ families of planes describe the morphology of the pentagonal dodecahedra (Figure 3, right), while the other planes are generated by symmetry. The full set of planes generated in this manner is a set of six indices to describe the facets parallel to the c -axis, $\{(1-10), (-110), (100), (-100), (010), (0-10)\}$, and a set of six indices describing facets that intersect the c -axis to cap the crystallite, $\{(401), (-40-1), (0-41), (04-1), (4-41), (4-4-1)\}$ (teal and violet, respectively, in Figure 3). Geometric overlays from

multiple angles enabled assignment of morphology, but it is important to stress that this assignment does not provide information about specific surface chemistry and is merely a recreation of the three-dimensional shape. Some care must be taken with this approach, as the method reconstructs polyhedra from two-dimensional projections of crystals oriented at many angles relative to the viewing axis. For example, nearly all information about faces intersecting the c -axis is lost when the crystals are aligned directly along the 3-fold axis (Figures S4 and S5). Given sufficient randomly distributed particles, crystallite morphology may be reconstructed with confidence.

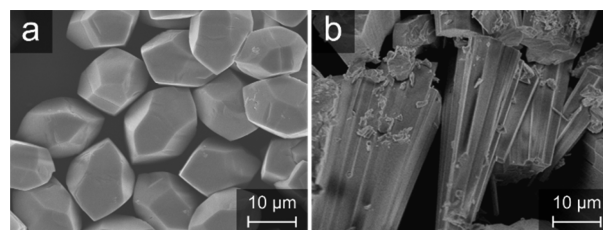


Figure 2. SEM images of $Co_2(dobdc)$ synthesized from H_4dobdc and cobalt(II) acetate in (a) 1:1 water/ethanol and (b) using a published single-crystal solvothermal route.³⁷

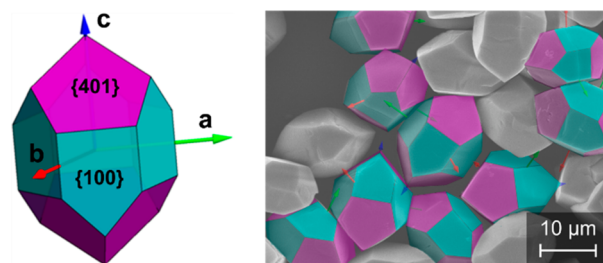


Figure 3. Illustration of the morphology of $Co_2(dobdc)$ pentagonal dodecahedra with axes and generating faces overlaid (left). Projection of this morphology onto the SEM image of $Co_2(dobdc)$ from Figure 2a, with crystallites arranged at different angles (right).

Non-Coordinating Buffers. Most solvothermal syntheses reported for $Co_2(dobdc)$ result in polydisperse mixtures containing rod-like crystallites extending along the c -axis.^{43–52} The ability to access homogeneous, low-aspect ratio crystallites as reported here is therefore notable and suggests that the nonbuffered synthesis route affords a level of morphological control that is typically absent in solvothermal reactions. A key difference between our synthesis and the typical literature solvothermal syntheses of MOF single crystals is the use of an acetate salt as the metal precursor, suggesting that acetate may play a role in determining crystallite shape. Previous reports of coordination modulation in the synthesis of various frameworks, including $Ni_2(dobdc)$ and $Mg_2(dobdc)$, have shown that acetate can interact with metal ions as a Lewis base, thereby influencing the interactions between the metal ions and linker molecules.^{65–69} By design, acetate here also acts as a Brønsted base to deprotonate the linker. However, pH also plays an important role in morphology,^{68,69} and it is impossible to know *a priori* if the presence of acetate is also important for the synthesis of narrow-dispersity, low-aspect ratio crystallites without eliminating acetate from the reaction. If the presence of acetate is required for uniform crystallites, it could be acting either as a director of crystallite shape through

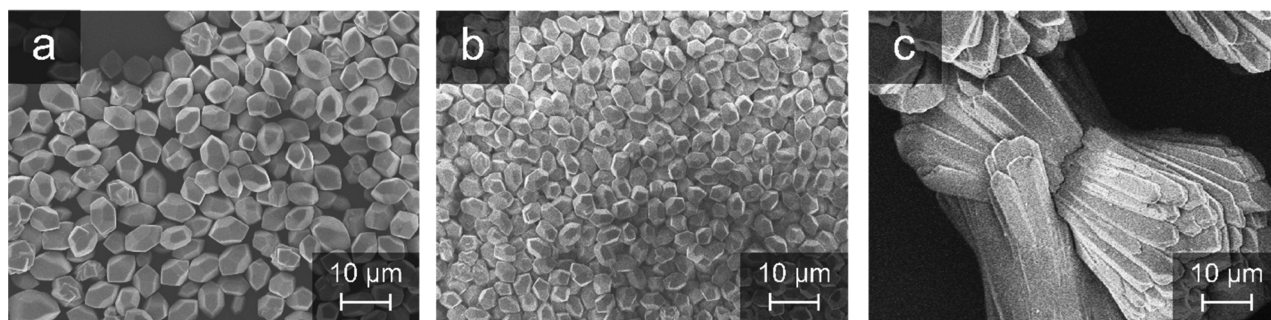


Figure 4. $\text{Co}_2(\text{dobdc})$ crystallites synthesized with (a) H_4dobdc and cobalt(II) acetate without buffer, (b) H_4dobdc and cobalt(II) acetate with MOPS buffer (pH = 7), and (c) H_4dobdc and cobalt(II) tetrafluoroborate with MOPS buffer.

metal coordination or as a pH-altering base, such that the consequent extent of linker deprotonation is optimal for generating the observed crystallite shape. The independent evaluation of both of these possibilities requires the use of a noncoordinating buffer in $\text{Co}_2(\text{dobdc})$ synthesis.

Toward this end, we first examined the effect of including a nominally noncoordinating buffer on crystallite morphology with acetate still present in solution. In general, the addition of a buffer will increase the ionic strength of the reaction solution while maintaining the pH at a constant value relative to the nonbuffered solution. The molecule 4-morpholinepropanesulfonic acid (MOPS)²⁸ was chosen as a suitable buffer for neutral-pH reaction conditions, given that it has a pK_a of 7.2 and that numerous studies have established that it interacts very weakly or negligibly with metal ions in solution.³² As a control to account for any metal ion–buffer interaction, the synthesis of $\text{Co}_2(\text{dobdc})$ was carried out using the same reaction conditions in the presence and absence of buffer near neutral pH (see the Supporting Information for details). In the presence of MOPS, the reaction mixture was maintained at a constant pH = 7, while the pH of the nonbuffered reaction decreased slightly from 6.7(1) to 5.5(1) as H_4dobdc was deprotonated. SEM images of the crystallites resulting from both reactions are shown in Figure 4a,b. Importantly, there is no discernible difference in the crystal morphology, suggesting that MOPS buffer may be used to control pH with negligible participation in metal complexation under these reaction conditions. Of note, it was also found that by carrying out the buffered framework synthesis in silanized glassware, the sensitivity of crystallite size and morphology to heating method is significantly minimized (Figure S6). Finally, there is no evidence of buffer incorporation into the framework via infrared spectroscopy (Figures S7 and S8).

The use of MOPS buffer further enabled the synthesis of $\text{Co}_2(\text{dobdc})$ in the presence of diverse cobalt(II) salts while maintaining neutral pH (Figures 4c and S9). Interestingly, substituting weakly coordinating tetrafluoroborate for acetate as the counteranion produces long, polycrystalline and polydisperse rods (Figure 4c), indicating that acetate plays a key role in controlling $\text{Co}_2(\text{dobdc})$ crystallite morphology. The use of cobalt(II) salts featuring anions with differing coordinating ability further resulted in uniform changes to the crystal morphology and apparent facets (Figure S9).

Using cobalt(II) acetate as the metal precursor, we also varied the reaction conditions by buffering the solution to pH values of 6.5 (using MOPS) or 5.5 and 6 (using 2-ethanesulfonic acid, MES). Although pH values ranging from 3 to 11 are accessible using noncoordinating buffers, cobalt

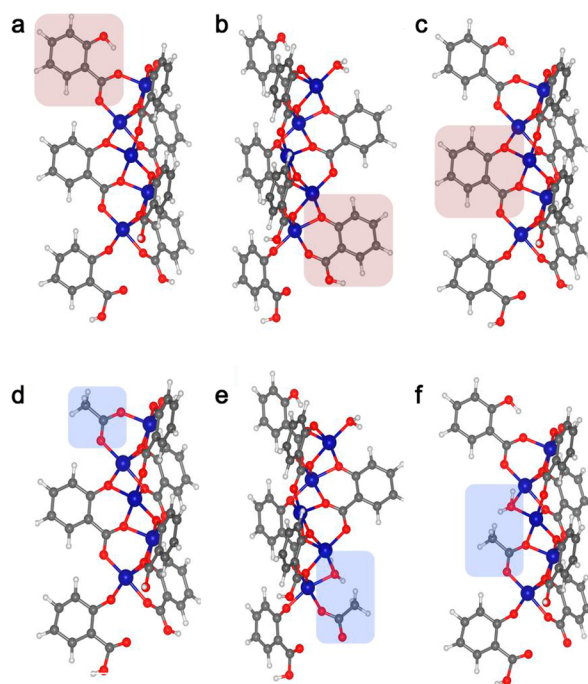


Figure 5. Helices used for DFT binding energy calculations. Co, O, C, and H atoms are shown in blue, red, gray, and white, respectively. (a–c) Replaced bidentate terminal, monodentate terminal, and middle-helix linker molecules are highlighted in red in parts a–c, respectively. (d–f) Target binding molecules are highlighted in blue. In part d, the linker is replaced by acetate, while in parts e and f, the linker is replaced by a combination of acetate and water.

hydroxide readily forms at pH ~ 8 ,⁷⁰ and reactions buffered below the pK_a of the carboxylate functionalities (<5) will not proceed in appreciable amounts. We found that decreasing the reaction pH increases crystal size and aspect ratio in the presence of acetate (Figure S10) but has no effect in the presence of tetrafluoroborate (Figure S11). Lowering the pH affects the protonation state of both acetate and H_4dobdc in solution and appears to slow overall formation. This result is also consistent with our observation that $\text{Co}_2(\text{dobdc})$ crystallites synthesized with cobalt(II) acetate without buffer are larger than crystallites synthesized with cobalt(II) acetate at pH 7 (Figure 4a and b). Thus, we can ascribe the pH-induced morphological changes to the $\text{Co}_2(\text{dobdc})$ crystallites to acetate protonation. Indeed, as acetate is protonated, it is less able to compete with the linker during crystal growth, leading to longer crystallites. This lack of coordination control also leads to greater morphological dispersity.

Computational Modeling. Density functional theory (DFT) calculations were carried out to study the competitive binding of acetate and dobdc^{4-} during $\text{Co}_2(\text{dobdc})$ crystallite formation, using a 125-atom helical cluster model consisting of five neighboring cobalt centers coordinated by seven linkers (Figure 5a–c). This cluster was constructed based on a previously reported 106-atom cluster developed to model $\text{C}_1\text{--C}_3$ hydrocarbon binding in $\text{Fe}_2(\text{dobdc})$.⁷¹ While both models feature five adjacent metal centers and seven linkers, a key difference in our cluster is that all of the linkers are derived from salicylic acid, whereas in the iron cluster, two of the linkers are truncated. The mixed-linker choice was suitable for the iron cluster because there is no substitution of the primary metal coordination sphere upon hydrocarbon binding, and the modeled gas adsorption site is far removed from the sites with truncated linkers. In contrast, a quantitative analysis of acetate and linker binding at various positions in the cobalt helix model requires the use of identical linkers. Finally, the coordination spheres of all unsaturated Co sites in our model were completed by a water molecule to better reflect the solvated environment in which the metal helices are formed.

Starting from the aforementioned 125-atom cluster, terminal or central linker molecules were replaced by bidentate acetate or monodentate acetate and a water molecule (Figure 5d–f). Binding energies were determined for each scenario and are given in Table 1. Binding of terminal bidentate- and terminal

Table 1. Computed Binding Energies (E_b) and Binding Energy Differences (ΔE) in kJ/mol for Terminal and Central Linkers and Acetate (or Acetate + Water) Molecules in the Cobalt Helix^a

Terminal coordination	E_b	ΔE_b
$[\text{C}_7\text{O}_3\text{H}_5]^-$	−85	
Bidentate $[\text{CH}_3\text{COO}]^-$	−113	−28
Monodentate $[\text{CH}_3\text{COO}]^- + \text{H}_2\text{O}$	−125	−40
Central coordination	E_b	ΔE_b
$[\text{C}_7\text{O}_3\text{H}_4]^{2-}$	−583	
Bidentate $[\text{CH}_3\text{COO}]^- + \text{H}_2\text{O}$	−598	−15

^a $\Delta E = E_b - E_b(\text{linker})$.

monodentate-bound acetate + water can compete favorably with binding of terminal linkers (Figure 5d,e). For instance, the binding of terminal bidentate acetate is 28 kJ/mol more favorable than terminal salicylate (binding energies of −113 versus −85 kJ/mol, respectively). The binding of terminal monodentate acetate + water is even more competitive, with a

binding energy of −125 kJ/mol. It is interesting to additionally compare terminal monodentate acetate + water binding to central bidentate acetate + water binding (Figure 5e,f). The computed binding energies indicate that competitive binding of terminal acetate + water is 25 kJ/mol more favorable than competitive binding of bidentate acetate + water in the center of the helix. Likewise, the binding of terminal acetate + water is 12 kJ/mol more favorable than competitive binding of terminal bidentate acetate. Thus, depending on the manner in which acetate binds, its competitive advantage over the linker can double. This finding has interesting implications for the mechanism of cluster growth in solution. While monodentate acetate and water binding is the most energetically competitive scenario, monodentate acetate may be dislodged more readily than a bidentate acetate. However, the monodentate binding scenario is likely stabilized by the coadsorption of water, which could also play a role in determining the kinetics of replacement. We note that in all cases, it is more favorable for acetate than for H_4dobdc to bind to Co, consistent with our hypothesis that acetate governs crystallite morphology by coordinating to the Co centers during crystal growth.

Counter Ions as Modulators for Controlled Morphologies. Given the evidence that acetate controls $\text{Co}_2(\text{dobdc})$ crystallite morphology via coordination during crystal growth, we sought to tune the morphology by changing the acetate binding strength. Acetate is readily modified by replacing the methyl group with more electron-donating or -withdrawing functionalities. The $\text{p}K_a$ value of each conjugate acid can be used as a proxy for coordination strength, given that the acidity of the carboxylate increases with the addition of electronegative substituents through inductive electron withdrawal.⁷² Formate, chloroacetate, and trichloroacetate were chosen as alternative counterions to probe the effects of binding strength on crystallite morphology. The $\text{p}K_a$ values of all the corresponding acids are <5 (Table S1),^{73,74} and thus each anion will be fully deprotonated in MOPS buffer solution. Cobalt(II) formate is commercially available, and cobalt(II) chloroacetate and cobalt(II) trichloroacetate were prepared via salt metathesis of cobalt carbonate and the corresponding haloacetic acid (see the Supporting Information). Some care needs to be taken in synthesizing and using trichloroacetate, which can undergo hydrolysis via the haloform reaction at elevated temperature in water. However, on the time scale and temperature scale of the $\text{Co}_2(\text{dobdc})$ synthesis, this side reaction is negligible.⁷⁵

The synthesis of $\text{Co}_2(\text{dobdc})$ starting from cobalt(II) acetate, formate, chloroacetate, or trichloroacetate in buffered solution produced monodisperse crystallites of varying aspect

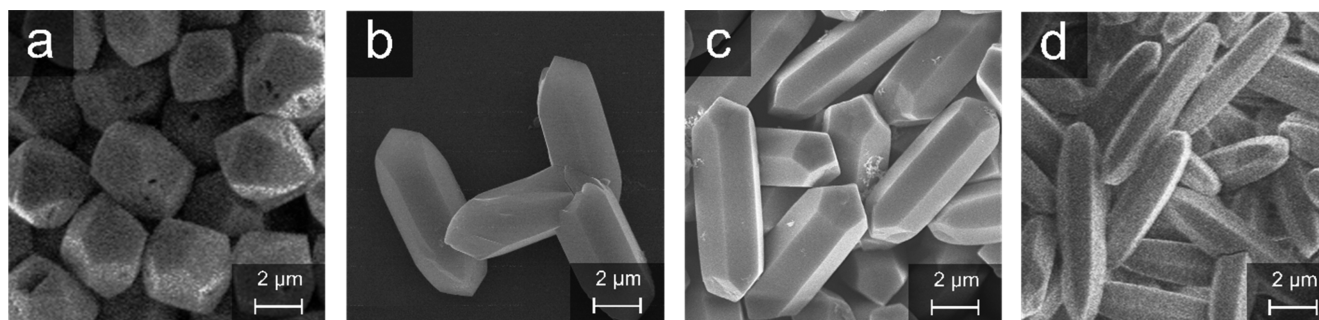


Figure 6. $\text{Co}_2(\text{dobdc})$ synthesized in water/ethanol buffered to pH 7 with different carboxylate metal salts: (a) cobalt(II) acetate, (b) cobalt(II) formate, (c) cobalt(II) chloroacetate, (d) cobalt(II) trichloroacetate.

ratios (Figure 6). Powder X-ray diffraction (PXRD) analysis of the resulting crystallites confirmed the formation of $\text{Co}_2(\text{dobdc})$ (Figure S12), and N_2 adsorption isotherms confirmed that all samples are highly porous. Quantification of modulator incorporation by ^1H nuclear magnetic resonance (NMR) across three batches of $\text{Co}_2(\text{dobdc})$ showed an average incorporation 0.01 ± 0.01 acetate: H_4dobdc and 0.06 ± 0.02 formate: $\text{H}_4(\text{dobdc})$ (molar ratios). No quantifiable chloroacetate was incorporated (Table S2). Together, the PXRD data, surface area measurements, and analysis of digested MOF by NMR indicate that the modulators did not significantly alter the bulk structure or defect density of $\text{Co}_2(\text{dobdc})$. The crystal aspect ratio increases in the order acetate < formate < chloroacetate < trichloroacetate and is therefore inversely related to the $\text{p}K_a$ of the corresponding conjugate acid (Table S1). Notably, because all reaction solutions were buffered to the same pH, the trend in crystal morphology can be ascribed directly to coordination modulation during growth. In particular, more electron-withdrawing groups diminish the ability of the carboxylate to compete with linker binding, resulting in longer crystallites. This observation indicates that the carboxylate-based modulators investigated preferentially bind along the c -axis of the crystal during crystal growth. Interestingly, the crystallite facets are the same for all crystals in the series, indicating that their surface energies are minimized irrespective of the competing anion (Figure S13). However, crystals prepared in the presence of trichloroacetate exhibit noticeably smoother facets than the other samples, suggesting that anion coordination may become negligible at very low conjugate acid $\text{p}K_a$ values. We note that the modulator does not need to be the sole counteranion in solution to observe these effects. Reaction conditions that utilized $\text{Co}(\text{NO}_3)_2$ starting material in conjunction with sodium acetate, sodium formate, or sodium chloroacetate gave rise to crystals of approximately the same size and aspect ratio as those synthesized with the coordination modulator as the anion in the Co starting material (Figure S14). Interestingly, the modulator concentration does not have a significant effect on the size or aspect ratio of the resulting crystals over a wide range of concentrations. By using $\text{Co}(\text{NO}_3)_2$ as a starting material, we were able to vary the acetate concentration in solution, and varying the acetate concentration across four concentrations ranging from 5 mM to 100 mM had a negligible impact on the resulting crystal size or aspect ratio (Figure S15). Furthermore, as discussed above, in the presence of even more weakly coordinating anions, morphological monodispersity is completely lost (Figure 4c). In general, the crystallite volume is similar across samples although it increases slightly with decreasing conjugate acid $\text{p}K_a$, which could imply a subtle lowering of the nucleation rate. Finally, we note the crystal yields are very high and nearly identical ($\sim 95\%$).

Aspect Ratio Dependent Diffusion of m -Xylene.

Morphological control of MOF crystals has direct consequences on system-level adsorbent performance. For instance, the diffusion of guest molecules within $\text{M}_2(\text{dobdc})$ frameworks is highly favored along the c -axis (i.e., through the hexagonal pores shown in Figure 1),⁵³ and thus the methods introduced in this study to control crystal aspect ratio should enable direct control over the diffusional path length under conditions wherein the limiting mass transfer resistance is intracrystalline diffusion. Specifically, we anticipated that gas diffusion will be faster in crystals with shorter dimensions along the c -axis

because those crystals would have a shorter diffusional path length (see the c -axis shown in Figure 3).

To test this hypothesis, we utilized zero length column (ZLC) chromatography to measure differences in the diffusion of m -xylene in the lowest and highest aspect ratio crystallites of $\text{Co}_2(\text{dobdc})$, prepared from cobalt(II) acetate and trichloroacetate, respectively, in MOPS buffer (see Figure 6 and the Supporting Information for details). ZLC chromatography is an established technique that enables differentiation between equilibrium- and kinetically controlled regimes and can be used to measure intracrystalline diffusion once the latter regime has been established.^{76,77} We chose m -xylene as a suitable probe molecule, given the high affinity of $\text{Co}_2(\text{dobdc})$ for C_8 alkylaromatics and the importance of their separation in industry.³⁹ The characteristic width of both the long and short aspect ratio crystals used for this experiment was $\sim 2.5 \mu\text{m}$ (Figure 6a,d), and thus their dimensions only differ along the c -axis.

In line with our hypothesis, m -xylene desorption from the longer crystals ($\sim 8 \mu\text{m}$ in length) exhibited a pronounced dependence on the purge gas flow rate, indicating that m -

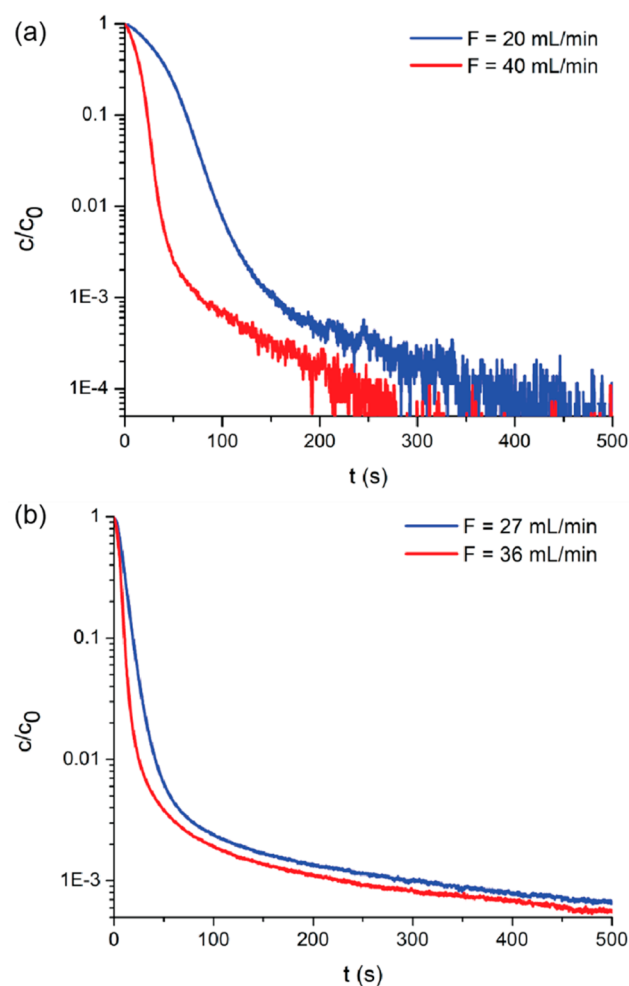


Figure 7. Comparison of desorption curves at two different He flow rates (F) for (a) long aspect ratio $\text{Co}_2(\text{dobdc})$ (path length = $2.5 \mu\text{m}$) and (b) the short aspect ratio $\text{Co}_2(\text{dobdc})$ crystallites; the steep drop-off is due to the nonlinear isotherm. See Supporting Information for detailed discussion of zero length column chromatography theory and experiments.

xylene diffusion in longer crystals is under kinetic control (Figure 7a). In contrast, the desorption rate in shorter crystals ($\sim 4 \mu\text{m}$ in length) was negligibly impacted by flow rate, even under the highest flow rates attainable, indicating that *m*-xylene diffusion in shorter crystals is under equilibrium control (Figure 7b). Additional details and discussion of the ZLC experiment and data analysis are given in the [Supporting Information](#). These results indicate that the shorter crystallites are better-suited for process use because the material selectivity is unaffected, while the adsorbate flux is increased due to a decrease in diffusional path length. More broadly, the ability to control MOF crystal morphology—and thereby adsorbate diffusion in MOFs—via modulated, buffered syntheses is a powerful new approach for the tailored synthesis of these adsorbents for industrially relevant applications.

CONCLUSIONS

By employing noncoordinating buffers in the synthesis of the metal–organic framework $\text{Co}_2(\text{dobdc})$, we have been able to deconvolute the effects of reaction pH and coordinating anion on crystal morphology. Theory and experiment both indicate that morphological control stems from coordinating anions in solution, which engage in anisotropic competitive binding during crystallite growth. The degree of interaction can be tuned by varying the electron density on the interacting functional group of the anion, allowing access to monodisperse sets of crystallites with varying aspect ratios. Diffusional studies indicate that path length control enables the minimization of diffusional resistances for the industrially important molecule *m*-xylene, highlighting the power of this synthetic approach for tuning framework crystallites to suit a given process. We anticipate that the high level of precision and rational control over MOF crystallite morphology demonstrated here can be extended beyond aqueous solvents to establish the use of noncoordinating buffers for precise pH control in nonaqueous and water-incompatible syntheses.

ASSOCIATED CONTENT

Supporting Information

The Supporting Information is available free of charge at <https://pubs.acs.org/doi/10.1021/jacs.1c00136>.

Experimental details, gas adsorption measurements, morphological indexing, DFT, additional crystal characterization, and ZLC details (PDF)

$\text{Co}_2(\text{dobdc})$ helix structures used in DFT calculations (XYZ)

AUTHOR INFORMATION

Corresponding Author

Jeffrey R. Long – Department of Chemical and Biomolecular Engineering, University of California, Berkeley, Berkeley, California 94720, United States; Department of Chemistry, University of California, Berkeley, Berkeley, California 94720, United States; Materials Sciences Division, Lawrence Berkeley National Laboratory, Berkeley, California 94720, United States; orcid.org/0000-0002-5324-1321; Email: jrlong@berkeley.edu

Authors

Kristen A. Colwell – Department of Chemical and Biomolecular Engineering, University of California, Berkeley, Berkeley, California 94720, United States

Megan N. Jackson – Department of Chemistry, University of California, Berkeley, Berkeley, California 94720, United States

Rodolfo M. Torres-Gavosto – Department of Chemistry, University of California, Berkeley, Berkeley, California 94720, United States

Sudi Jawahery – Department of Chemical and Biomolecular Engineering, University of California, Berkeley, Berkeley, California 94720, United States; Laboratory of Molecular Simulation (LSMO), Institut des Sciences et Ingénierie Chimiques, Valais, École Polytechnique Fédérale de Lausanne (EPFL), CH-1951 Sion, Switzerland; orcid.org/0000-0001-9950-6199

Bess Vlaisavljevich – Department of Chemistry, University of South Dakota, Vermillion, South Dakota 57069, United States; orcid.org/0000-0001-6065-0732

Joseph M. Falkowski – Corporate Strategic Research, ExxonMobil Research and Engineering Company, Annandale, New Jersey 08801, United States; orcid.org/0000-0002-3221-2548

Berend Smit – Department of Chemical and Biomolecular Engineering, University of California, Berkeley, Berkeley, California 94720, United States; Laboratory of Molecular Simulation (LSMO), Institut des Sciences et Ingénierie Chimiques, Valais, École Polytechnique Fédérale de Lausanne (EPFL), CH-1951 Sion, Switzerland; orcid.org/0000-0003-4653-8562

Simon C. Weston – Corporate Strategic Research, ExxonMobil Research and Engineering Company, Annandale, New Jersey 08801, United States; orcid.org/0000-0002-7439-5055

Complete contact information is available at:

<https://pubs.acs.org/doi/10.1021/jacs.1c00136>

Notes

The authors declare the following competing financial interest(s): The authors declare the following competing financial interest(s): K.A.C., R.M.T.-G., J.M.F., S.C.W., and J.R.L. are inventors on patent application 20200101439, submitted by The Regents of the University of California and the ExxonMobil Research and Engineering Company, that covers the synthetic methods described in this work.

ACKNOWLEDGMENTS

This work was supported by ExxonMobil Research and Engineering Company. The ZLC instrument was purchased with funding from the Center for Gas Separations, an Energy Frontier Research Center funded by the U.S. Department of Energy, Office of Science, Office of Basic Energy Sciences (DESC0001015), which also funded the computational portion of this research (S.J., B.V., and B.S.). We thank the National Science Foundation for graduate fellowship funding of R.T.-G. and S.J., the UC Berkeley Chancellor's Fellowship for additional funding of R.T.-G.. M.N.J. is supported by an Arnold O. Beckman postdoctoral fellowship. We further thank the University of South Dakota for startup funding of B.V. and Dr. Katie R. Meihaus for editorial assistance.

REFERENCES

(1) Li, J.-R.; Kuppler, R. J.; Zhou, H.-C. Selective Gas Adsorption and Separation in Metal–Organic Frameworks. *Chem. Soc. Rev.* **2009**, *38*, 1477–1504.

- (2) Zhou, H.-C.; Long, J. R.; Yaghi, O. M. Introduction to Metal–Organic Frameworks. *Chem. Rev.* **2012**, *112*, 673–674.
- (3) McDonald, T. M.; Mason, J. A.; Kong, X.; Bloch, E. D.; Gygi, D.; Dani, A.; Crocellà, V.; Giordanino, F.; Odoh, S. O.; Drisdell, W. S.; Vlaisavljevich, B.; Dzubak, A. L.; Poloni, R.; Schnell, S. K.; Planas, N.; Lee, K.; Pascal, T.; Wan, L. F.; Prendergast, D.; Neaton, J. B.; Smit, B.; Kortright, J. B.; Gagliardi, L.; Bordiga, S.; Reimer, J. A.; Long, J. R. Cooperative Insertion of CO₂ in Diamine-Appended Metal–Organic Frameworks. *Nature* **2015**, *519*, 303–308.
- (4) Lee, J.; Farha, O. K.; Roberts, J.; Scheidt, K. A.; Nguyen, S. T.; Hupp, J. T. Metal–Organic Framework Materials as Catalysts. *Chem. Soc. Rev.* **2009**, *38*, 1450–1459.
- (5) Xiao, D. J.; Bloch, E. D.; Mason, J. A.; Queen, W. L.; Hudson, M. R.; Planas, N.; Borycz, J.; Dzubak, A. L.; Verma, P.; Lee, K.; Bonino, F.; Crocellà, V.; Yano, J.; Bordiga, S.; Truhlar, D. G.; Gagliardi, L.; Brown, C. M.; Long, J. R. Oxidation of Ethane to Ethanol by N₂O in a Metal–Organic Framework with Coordinatively Unsaturated Iron(II) Sites. *Nat. Chem.* **2014**, *6*, 590–595.
- (6) Corma, A.; García, H.; Llabrés i Xamena, F. X. Engineering Metal Organic Frameworks for Heterogeneous Catalysis. *Chem. Rev.* **2010**, *110*, 4606–4655.
- (7) Horcajada, P.; Chalati, T.; Serre, C.; Gillet, B.; Sebrie, C.; Baati, T.; Eubank, J. F.; Heurtaux, D.; Clayette, P.; Kreuz, C.; Chang, J.-S.; Hwang, Y. K.; Marsaud, V.; Bories, P.-N.; Cynober, L.; Gil, S.; Férey, G.; Couvreur, P.; Gref, R. Porous Metal–Organic-Framework Nanoscale Carriers as a Potential Platform for Drug Delivery and Imaging. *Nat. Mater.* **2010**, *9*, 172–178.
- (8) Levine, D. J.; Kapelewski, M. T.; Keitz, B. K.; Oktawiec, J.; Reed, D. A.; Mason, J. A.; H Jiang, H. Z.; Colwell, K. A.; Legendre, C. M.; FitzGerald, S. A.; Long, J. R. Olsalazine-Based Metal–Organic Frameworks as Biocompatible Platforms for H₂ Adsorption and Drug Delivery. *J. Am. Chem. Soc.* **2016**, *138*, 10143–10150.
- (9) Rosi, N. L.; Eckert, J.; Eddaoudi, M.; Vodak, D. T.; Kim, J.; O’Keeffe, M.; Yaghi, O. M. Hydrogen Storage in Microporous Metal–Organic Frameworks. *Science* **2003**, *300*, 1127–1129.
- (10) Mason, J. A.; Oktawiec, J.; Taylor, M. K.; Hudson, M. R.; Rodriguez, J.; Bachman, J. E.; Gonzalez, M. I.; Cervellino, A.; Guagliardi, A.; Brown, C. M.; Llewellyn, P. L.; Masciocchi, N.; Long, J. R. Methane Storage in Flexible Metal–Organic Frameworks with Intrinsic Thermal Management. *Nature* **2015**, *527*, 357–361.
- (11) Gassensmith, J. J.; Kim, J. Y.; Holcroft, J. M.; Farha, O. K.; Stoddart, J. F.; Hupp, J. T.; Jeong, N. C. A Metal–Organic Framework-Based Material for Electrochemical Sensing of Carbon Dioxide. *J. Am. Chem. Soc.* **2014**, *136*, 8277–8282.
- (12) Chen, L.; Ye, J.-W.; Wang, H.-P.; Pan, M.; Yin, S.-Y.; Wei, Z.-W.; Zhang, L.-Y.; Wu, K.; Fan, Y.-N.; Su, C.-Y. Ultrafast Water Sensing and Thermal Imaging by a Metal–Organic Framework with Switchable Luminescence. *Nat. Commun.* **2017**, *8*, 15985.
- (13) Allendorf, M. D.; Houk, R. J. T.; Andruszkiewicz, L.; Talin, A. A.; Pikarsky, J.; Choudhury, A.; Gall, K. A.; Hesketh, P. J. Stress-Induced Chemical Detection Using Flexible Metal–Organic Frameworks. *J. Am. Chem. Soc.* **2008**, *130*, 14404–14405.
- (14) Rousseau, R. W. *Handbook of Separation Process Technology*; J. Wiley, 1987, 669–672.
- (15) Stock, N.; Biswas, S. Synthesis of Metal–Organic Frameworks (MOFs): Routes to Various MOF Topologies, Morphologies, and Composites. *Chem. Rev.* **2012**, *112*, 933–969.
- (16) Umemura, A.; Diring, S.; Furukawa, S.; Uehara, H.; Tsuruoka, T.; Kitagawa, S. Morphology Design of Porous Coordination Polymer Crystals by Coordination Modulation. *J. Am. Chem. Soc.* **2011**, *133*, 15506–15513.
- (17) Diring, S.; Furukawa, S.; Takashima, Y.; Tsuruoka, T.; Kitagawa, S. Controlled Multiscale Synthesis of Porous Coordination Polymer in Nano/Micro Regimes. *Chem. Mater.* **2010**, *22*, 4531–4538.
- (18) Hermes, S.; Witte, T.; Hikov, T.; Zacher, D.; Bahnmüller, S.; Langstein, G.; Huber, K.; Fischer, R. A. Trapping Metal–Organic Framework Nanocrystals: An in-Situ Time-Resolved Light Scattering Study on the Crystal Growth of MOF-5 in Solution. *J. Am. Chem. Soc.* **2007**, *129*, 5324–5325.
- (19) Cho, W.; Lee, H. J.; Oh, M. Growth-Controlled Formation of Porous Coordination Polymer Particles. *J. Am. Chem. Soc.* **2008**, *130*, 16943–16946.
- (20) Pachfule, P.; Shinde, D.; Majumder, M.; Xu, Q. Fabrication of Carbon Nanorods and Graphene Nanoribbons from a Metal–Organic Framework. *Nat. Chem.* **2016**, *8*, 718–724.
- (21) Guo, H.; Zhu, Y.; Wang, S.; Su, S.; Zhou, L.; Zhang, H. Combining Coordination Modulation with Acid–Base Adjustment for the Control over Size of Metal–Organic Frameworks. *Chem. Mater.* **2012**, *24*, 444–450.
- (22) Shan, B.; James, J. B.; Armstrong, M. R.; Close, E. C.; Letham, P. A.; Nikkiah, K.; Lin, Y. S.; Mu, B. Influences of Deprotonation and Modulation on Nucleation and Growth of UiO-66: Intergrowth and Orientation. *J. Phys. Chem. C* **2018**, *122*, 2200–2206.
- (23) Zhao, Y.; Zhang, Q.; Li, Y.; Zhang, R.; Lu, G. Large-Scale Synthesis of Monodisperse UiO-66 Crystals with Tunable Sizes and Missing Linker Defects via Acid/Base Co-Modulation. *ACS Appl. Mater. Interfaces* **2017**, *9*, 15079–15085.
- (24) Barthel, J. M. G.; Krienke, H.; Kunz, W. *Physical Chemistry of Electrolyte Solutions: Modern Aspects*; Steinkopff, Darmstadt, and Springer: New York, 1998, 183–260.
- (25) *Activity Coefficients in Electrolyte Solutions*, 2nd ed.; Pitzer, K. S., Ed.; CRC Press: Boca Raton, FL, 2018, 29–154, 279–434.
- (26) Kielland, J. Individual Activity Coefficients of Ions in Aqueous Solutions. *J. Am. Chem. Soc.* **1937**, *59*, 1675–1678.
- (27) Buncel, E.; Symons, E. A. The Inherent Instability of Dimethylformamide–Water Systems Containing Hydroxide Ion. *J. Chem. Soc. D* **1970**, *0*, 164–165.
- (28) Good, N. E.; Winget, G. D.; Winter, W.; Connolly, T. N.; Izawa, S.; Singh, R. M. M. Hydrogen Ion Buffers for Biological Research. *Biochemistry* **1966**, *5*, 467–477.
- (29) Holm, R. H.; Kennepohl, P.; Solomon, E. I. Structural and Functional Aspects of Metal Sites in Biology. *Chem. Rev.* **1996**, *96*, 2239–2314.
- (30) Aqvist, J.; Warshel, A. Free Energy Relationships in Metalloenzyme-Catalyzed Reactions. Calculations of the Effects of Metal Ion Substitutions in Staphylococcal Nuclease. *J. Am. Chem. Soc.* **1990**, *112*, 2860–2868.
- (31) Aqvist, J.; Warshel, A. Computer Simulation of the Initial Proton Transfer Step in Human Carbonic Anhydrase I. *J. Mol. Biol.* **1992**, *224*, 7–14.
- (32) Ferreira, C. M. H.; Pinto, I. S. S.; Soares, E. V.; Soares, H. M. V. M. (Un)Suitability of the Use of PH Buffers in Biological, Biochemical and Environmental Studies and Their Interaction with Metal Ions – a Review. *RSC Adv.* **2015**, *5*, 30989–31003.
- (33) Kandedgedara, A.; Rorabacher, D. B. Noncomplexing Tertiary Amines as “Better” Buffers Covering the Range of PH 3–11. Temperature Dependence of Their Acid Dissociation Constants. *Anal. Chem.* **1999**, *71*, 3140–3144.
- (34) Yu, Q.; Kandedgedara, A.; Xu, Y.; Rorabacher, D. B. Avoiding Interferences from Good’s Buffers: A Contiguous Series of Non-complexing Tertiary Amine Buffers Covering the Entire Range of PH 3–11. *Anal. Biochem.* **1997**, *253*, 50–56.
- (35) Rosi, N. L.; Kim, J.; Eddaoudi, M.; Chen, B.; Yaghi, O. M. Rod Packings and Metal–Organic Frameworks Constructed from Rod-Shaped Secondary Building Units. *J. Am. Chem. Soc.* **2005**, *127*, 1504–1518.
- (36) Rowsell, J. L. C.; Yaghi, O. M. Effects of Functionalization, Catenation, and Variation of the Metal Oxide and Organic Linking Units on the Low-Pressure Hydrogen Adsorption Properties of Metal–Organic Frameworks. *J. Am. Chem. Soc.* **2006**, *128*, 1304–1315.
- (37) Caskey, S. R.; Wong-Foy, A. G.; Matzger, A. J. Dramatic Tuning of Carbon Dioxide Uptake via Metal Substitution in a Coordination Polymer with Cylindrical Pores. *J. Am. Chem. Soc.* **2008**, *130*, 10870–10871.

- (38) Díaz-García, M.; Sánchez-Sánchez, M. Synthesis and Characterization of a New Cd-Based Metal-Organic Framework Isostructural with MOF-74/CPO-27 Materials. *Microporous Mesoporous Mater.* **2014**, *190*, 248–254.
- (39) Yang, D.-A.; Cho, H.-Y.; Kim, J.; Yang, S.-T.; Ahn, W.-S. CO₂ Capture and Conversion Using Mg-MOF-74 Prepared by a Sonochemical Method. *Energy Environ. Sci.* **2012**, *5*, 6465–6473.
- (40) Peng, Y.; Krungleviciute, V.; Eryazici, I.; Hupp, J. T.; Farha, O. K.; Yildirim, T. Methane Storage in Metal–Organic Frameworks: Current Records, Surprise Findings, and Challenges. *J. Am. Chem. Soc.* **2013**, *135*, 11887–11894.
- (41) Kapelewski, M. T.; Runčevski, T.; Tarver, J. D.; Jiang, H. Z. H.; Hurst, K. E.; Parilla, P. A.; Ayala, A.; Gennett, T.; FitzGerald, S. A.; Brown, C. M.; Long, J. R. Record High Hydrogen Storage Capacity in the Metal–Organic Framework Ni₂(m-dobdc) at Near-Ambient Temperatures. *Chem. Mater.* **2018**, *30*, 8179–8189.
- (42) Sumida, K.; Brown, C. M.; Herm, Z. R.; Chavan, S.; Bordiga, S.; Long, J. R. Hydrogen Storage Properties and Neutron Scattering Studies of Mg₂(dobdc)—a Metal–Organic Framework with Open Mg²⁺ Adsorption Sites. *Chem. Commun.* **2011**, *47*, 1157–1159.
- (43) Gonzalez, M. I.; Kapelewski, M. T.; Bloch, E. D.; Milner, P. J.; Reed, D. A.; Hudson, M. R.; Mason, J. A.; Barin, G.; Brown, C. M.; Long, J. R. Separation of Xylene Isomers through Multiple Metal Site Interactions in Metal–Organic Frameworks. *J. Am. Chem. Soc.* **2018**, *140*, 3412–3422.
- (44) Chmelik, C.; Mundstock, A.; Dietzel, P. D. C.; Caro, J. Idiosyncrasies of Co₂(dhtp): In Situ-Annealing by Methanol. *Microporous Mesoporous Mater.* **2014**, *183*, 117–123.
- (45) Haque, E.; Jhung, S. H. Synthesis of Isostructural Metal–Organic Frameworks, CPO-27s, with Ultrasound, Microwave, and Conventional Heating: Effect of Synthesis Methods and Metal Ions. *Chem. Eng. J.* **2011**, *173* (3), 866–872.
- (46) Yan, W.; Guo, Z.; Xu, H.; Lou, Y.; Chen, J.; Li, Q. Downsizing Metal–Organic Frameworks with Distinct Morphologies as Cathode Materials for High-Capacity Li–O₂ Batteries. *Mater. Chem. Front.* **2017**, *1*, 1324–1330.
- (47) Chen, J.; Mu, X.; Du, M.; Lou, Y. Porous Rod-Shaped Co₃O₄ Derived from Co-MOF-74 as High-Performance Anode Materials for Lithium Ion Batteries. *Inorg. Chem. Commun.* **2017**, *84*, 241–245.
- (48) Tang, J.; Yamauchi, Y. MOF Morphologies in Control. *Nat. Chem.* **2016**, *8*, 638–639.
- (49) Vornholt, S. M.; Henkelis, S. E.; Morris, R. E. Low Temperature Synthesis Study of Metal–Organic Framework CPO-27: Investigating Metal, Solvent and Base Effects down to –78 °C. *Dalton Trans.* **2017**, *46*, 8298–8303.
- (50) Cattaneo, D.; Warrender, S. J.; Duncan, M. J.; Castledine, R.; Parkinson, N.; Haley, I.; Morris, R. E. Water Based Scale-up of CPO-27 Synthesis for Nitric Oxide Delivery. *Dalton Trans.* **2016**, *45*, 618–629.
- (51) Bétard, A.; Zacher, D.; Fischer, R. A. Dense and Homogeneous Coatings of CPO-27-M Type Metal–Organic Frameworks on Alumina Substrates. *CrystEngComm* **2010**, *12*, 3768–3772.
- (52) Jiang, H.; Wang, Q.; Wang, H.; Chen, Y.; Zhang, M. Temperature Effect on the Morphology and Catalytic Performance of Co-MOF-74 in Low-Temperature NH₃-SCR Process. *Catal. Commun.* **2016**, *80*, 24–27.
- (53) Forse, A. C.; Colwell, K. A.; Gonzalez, M. I.; Benders, S.; Torres-Gavosto, R. M.; Blümich, B.; Reimer, J. A.; Long, J. R. Influence of Pore Size on Carbon Dioxide Diffusion in Two Isorecticular Metal–Organic Frameworks. *Chem. Mater.* **2020**, *32*, 3570–3576.
- (54) Cadot, S.; Veyre, L.; Luneau, D.; Farrusseng, D.; Alessandra Quadrelli, E. A Water-Based and High Space-Time Yield Synthetic Route to MOF Ni₂(dhtp) and Its Linker 2,5-dihydroxyterephthalic Acid. *J. Mater. Chem. A* **2014**, *2*, 17757–17763.
- (55) Sánchez-Sánchez, M.; Getachew, N.; Díaz, K.; Díaz-García, M.; Chebude, Y.; Díaz, I. Synthesis of Metal–Organic Frameworks in Water at Room Temperature: Salts as Linker Sources. *Green Chem.* **2015**, *17*, 1500–1509.
- (56) Dietzel, P. D. C.; Blom, R.; Fjellvåg, H. Base-Induced Formation of Two Magnesium Metal-Organic Framework Compounds with a Bifunctional Tetratopic Ligand. *Eur. J. Inorg. Chem.* **2008**, *2008*, 3624–3632.
- (57) Dietzel, P. D. C.; Besikiotis, V.; Blom, R. Application of Metal–Organic Frameworks with Coordinatively Unsaturated Metal Sites in Storage and Separation of Methane and Carbon Dioxide. *J. Mater. Chem.* **2009**, *19*, 7362–7370.
- (58) Dietzel, P. D. C.; Panella, B.; Hirscher, M.; Blom, R.; Fjellvåg, H. Hydrogen Adsorption in a Nickel Based Coordination Polymer with Open Metal Sites in the Cylindrical Cavities of the Desolvated Framework. *Chem. Commun.* **2006**, *1*, 959–961.
- (59) Bates, R. G.; Paabo, M.; Robinson, R. A. Interpretation of pH Measurements in Alcohol–Water Solvents. *J. Phys. Chem.* **1963**, *67* (9), 1833–1838.
- (60) Mussini, P. R.; Mussini, T.; Rondinini, S. Reference Value Standards and Primary Standards for pH Measurements in D₂O and Aqueous–Organic Solvent Mixtures: New Accessions and Assessments. *Pure Appl. Chem.* **1997**, *69*, 1007–1014.
- (61) Rondinini, S. pH Measurements in Non-Aqueous and Aqueous–Organic Solvents - Definition of Standard Procedures. *Anal. Bioanal. Chem.* **2002**, *374*, 813–816.
- (62) Tranchemontagne, D. J.; Hunt, J. R.; Yaghi, O. M. Room Temperature Synthesis of Metal-Organic Frameworks: MOF-5, MOF-74, MOF-177, MOF-199, and IRMOF-0. *Tetrahedron* **2008**, *64*, 8553–8557.
- (63) Garzón-Tovar, L.; Carné-Sánchez, A.; Carbonell, C.; Imaz, I.; Maspoch, D. Optimised Room Temperature, Water-Based Synthesis of CPO-27-M Metal–Organic Frameworks with High Space-Time Yields. *J. Mater. Chem. A* **2015**, *3*, 20819–20826.
- (64) Janner, A.; Janssen, T. From Crystal Morphology to Molecular and Scale Crystallography. *Phys. Scr.* **2015**, *90*, 088007.
- (65) Forgan, R. S. Modulated Self-Assembly of Metal–Organic Frameworks. *Chem. Sci.* **2020**, *11*, 4546–4562.
- (66) Marshall, C. R.; Staudhammer, S.; Brozek, C. Experimental Evidence for a General Model of Modulated MOF Nanoparticle Growth. *Chem. Sci.* **2020**, *11*, 11539–11547.
- (67) McGuire, C. V.; Forgan, R. S. The Surface Chemistry of Metal–Organic Frameworks. *Chem. Commun.* **2015**, *51*, 5199–5217.
- (68) Wu, C.; Chou, L.-Y.; Long, L.; Si, X.; Lo, W.-S.; Tsung, C.-K.; Li, T. Structural Control of Uniform MOF-74 Microcrystals for the Study of Adsorption Kinetics. *ACS Appl. Mater. Interfaces* **2019**, *11*, 35820–35826.
- (69) Rosnes, M. H.; Nesse, F. S.; Opitz, M.; Dietzel, P. D. C. Morphology Control in Modulated Synthesis of Metal-Organic Framework CPO-27. *Microporous Mesoporous Mater.* **2019**, *275*, 207–213.
- (70) Pourbaix, M. *Atlas of Electrochemical Equilibria in Aqueous Solutions*; NACE International: TX, 1974.
- (71) Verma, P.; Xu, X.; Truhlar, D. G. Adsorption on Fe-MOF-74 for C1–C3 Hydrocarbon Separation. *J. Phys. Chem. C* **2013**, *117*, 12648–12660.
- (72) Lewis, G. N. *Valence and the Structure of Atoms and Molecules*; The Chemical Catalog Company: New York, 1923, 79–87.
- (73) *Determination of Organic Structures by Physical Methods*; Braude, E. A., Nachod, F. C., Eds.; Elsevier, 1955, 567–662.
- (74) Dippy, J. F. J.; Hughes, S. R. C.; Rozanski, A. The Dissociation Constants of Some Symmetrically Disubstituted Succinic Acids. *J. Chem. Soc.* **1959**, 2492–2498.
- (75) Verhoek, F. H. The Kinetics of the Decomposition of the Trichloroacetates in Various Solvents. *J. Am. Chem. Soc.* **1934**, *56*, 571–577.
- (76) Eic, M.; Ruthven, D. M. A New Experimental Technique for Measurement of Intracrystalline Diffusivity. *Zeolites* **1988**, *8*, 40–45.
- (77) Brandani, S.; Ruthven, D. M. Analysis of ZLC Desorption Curves for Liquid Systems. *Adsorption* **1995**, *50*, 2055–2059.